PAPER

Nanotextured alpha Ni(II)–Co(II) hydroxides as supercapacitive active phases†

Nicolás Arencibia,[a] Víctor Oestreicher,[a] Federico A. Viva*[b] and Matías Jobbágy*[ac]

A family of monophasic nanoplatelets of Ni(II)–Co(II) layered hydroxides, were obtained by a one-pot room temperature homogeneous alkalinization driven by the the epoxide route with glycidol. Both cations precipitate in the form of solid solutions, giving the general formula $Ni_{1-x}Co_x(OH)_{2-y}Cl_y \cdot nH_2O$. Co(II)-rich samples developed the simonkolleite-like alpha structure in which cations can adopt either octahedral (Oh) or tetrahedral (Td) environments, according to the formula $(Ni,Co)^{Oh}_{1-x}Co^{Td}_{2x}(OH)_{2-2x}(Cl)_{2x} \cdot nH_2O$. Ni(II)-rich ones resulted in ill-crystallized turbostratic $(Ni,Co)_{1-x}(OH)_{2-x}(Cl)_x \cdot nH_2O$. Despite the inherent differences in the crystallochemical nature of theses phases, electrochemical measurements depict a monotonous behavior in terms of their capacitance. An optimum performance was observed for samples with $X_{Ni(II)} = 0.83$ under most of the experimental conditions explored. This sample reaches a maximum specific capacitance of 2091 F g^{-1}, registered at a discharge current density of 0.5 A g^{-1}, while an energy density of 80.7 W h kg^{-1} was recorded at a power density of 960.4 W kg^{-1}.

Introduction

The development of advanced platforms for energy production and storage is a permanent source of inspiration for those scientists devoted to chemistry of applied nanomaterials. Among the various electrochemical-based power sources, electrochemical capacitors (EC), also known as supercapacitors, are a competitive alternative due to their advantages in energy storage applications, such as high power densities and long cyclic lifetime. In particular, water based supercapacitors present high safety and low price besides being environmentally friendly.[1,2] Typically, these devices are based on the assembly of electroactive phases, able to develop faradic processes, dispersed at the nanoscale within suitable conductive substrates.[1,3–6] Among the accepted electroactive phases,[7] multicationic transition metal oxides[8] or hydroxides[9] play a key role in the race for efficiency in aqueous-based supercapacitors.[10–14] Binary Ni(II)–Co(II) compounds[15] were recently explored with special attention focused on hydroxylated phases.[16–18] The homogeneous alkalinization driven by the controlled thermal hydrolysis of hexamethylenetetramine (HMT),[18] formamide[19] or urea[20,21] succeeded in the preparation of monophasic layered

hydroxides, including Ni(II)–Co(II) phases.[21–26] However, these hydrothermal procedures, favor recrystallization process, with the subsequent loss of desirable metastable reactive phases.[18] Eventually, molecular spacers can be added to develop reactive architectures.[27,28] More recently it was demonstrated that several M(II) as well as M(II)–Al(III) LDH's can be obtained through chloride assisted epoxide's ring opening in aqueous solutions at 298 K, a mild method inherently free of carbonated or oxidized side-products.[29] The present study explores the one pot preparation of monophasic Ni(II)–Co(II) hydroxides obeying to the general formula $Ni_{1-x}Co_x(OH)_{2-y}Cl_y \cdot nH_2O$ and their crystalline nature. The electrochemical behavior is systematically explored along the whole range of Ni(II) to Co(II) ratio, finding a well-defined optimum capacity.

Results and discussion

Room-temperature homogeneous precipitation of several M(II) hydroxilated phases, including Ni(II) or Co(II) ones, can be driven by epoxide ring opening. It was reported that several epoxides are reactive enough to drive this reaction, however glycidol was chosen instead of the commonly employed propylene oxide[30–34] due to is higher boiling point, that makes it easy to handle at room temperature, preventing losses due to evaporation and subsequent harmful inhalations.[35] Fig. 1 presents the precipitation pH profiles of bare Co(II) or Ni(II) solutions (labeled as samples Ni0 and Ni100, respectively) as well as a solution containing an equimolar mixture of Co(II) and Ni(II), labeled as sample Ni50. The precipitation of sample Ni0 results in a pH plateau fixed at value of 8.2; sample Ni100 develop an analogous profile,

[a]INQUIMAE-DQIAQF, Facultad de Ciencias Exactas y Naturales, Universidad de Buenos Aires, Ciudad Universitaria, Pab. II, C1428EHA, Buenos Aires, Argentina. E-mail: jobbag@qi.fcen.uba.ar

[b]Departamento de Física de la Materia Condensada, Centro Atómico Constituyentes, Comisión Nacional de Energía Atómica, Av. General Paz 1499, B1650KNA, Buenos Aires, Argentina. E-mail: viva@tandar.cnea.gov.ar

[c]Centro Interdisciplinario de Nanociencia y Nanotecnología, Argentina

† Electronic supplementary information (ESI) available. See DOI: 10.1039/c6ra27839f
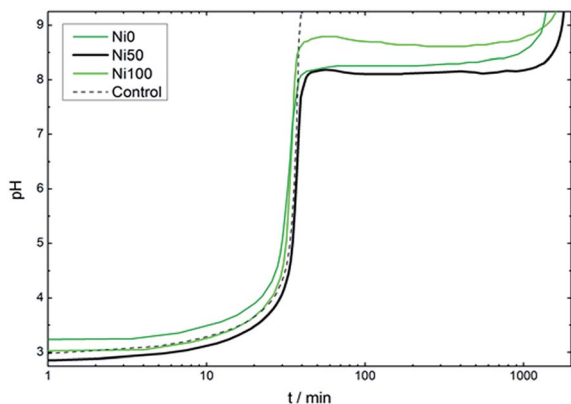
Fig. 1 Evolution of pH along the precipitation of samples Ni0, Ni50 and Ni100. Dotted line indicates the control alkalinization curve in the absence of Ni(II) or Co(II) cations.

except for an initial smooth pH overshoot reaching a value of 8.5 indicating a single massive nucleation event followed by a precipitation plateau fixed at pH = 8.4.[36] The equimolar mixture of Co(II) and Ni(II), labeled Ni50, depicts a precipitation plateau fixed at pH = 8.1. The lower value recorded respect to bare Ni(II) or Co(II) solutions (samples Ni100 and

Ni0, respectively) indicates the coprecipitation of both cations in a less soluble binary phase.

SEM images of the obtained solids are shown in Fig. 2, revealing textural differences depending on the composition. Starting from sample Ni0, rose-like aggregates of well developed hexagonal platelets can be observed with no signs of amorphous material (see ESI Fig. S1†). The high aspect ratio observed in each hexagonal crystalline domains results from the fast growth along the xy plane respect to the c direction.[29] The rose-like morphology obeys to the growth mechanism from a central seed depicted for related layered phases.[37] Increasing Ni(II) contents resulted in smaller aggregates composed of particles with less defined geometries; Ni(II)-rich samples resulted in spheroidal aggregates of corrugated flakes with no sharp corners (see ESI Fig. S1†).

The PXRD patterns recorded for all samples are depicted in Fig. 3, revealing a layered nature, irrespective of composition or texture. Samples Ni0 to Ni66 adopted the simonkolleite-like structure,[38] evidenced by the characteristic reflections recorded between 30 and 65 degrees.[39] This phase, depicted by the general formula $Co^{Oh}_{1-x}Co^{Td}_{2x}(OH)_{2-2x}(Cl)_{2x}\cdot0.46H_2O$, holds a main fraction of octahedral Co(II) centers, Co^{Oh}, belonging to an hexagonal cationic arrange. Certain Co^{Oh} positions within each layer are vacant and these sites are occupied by a couple of
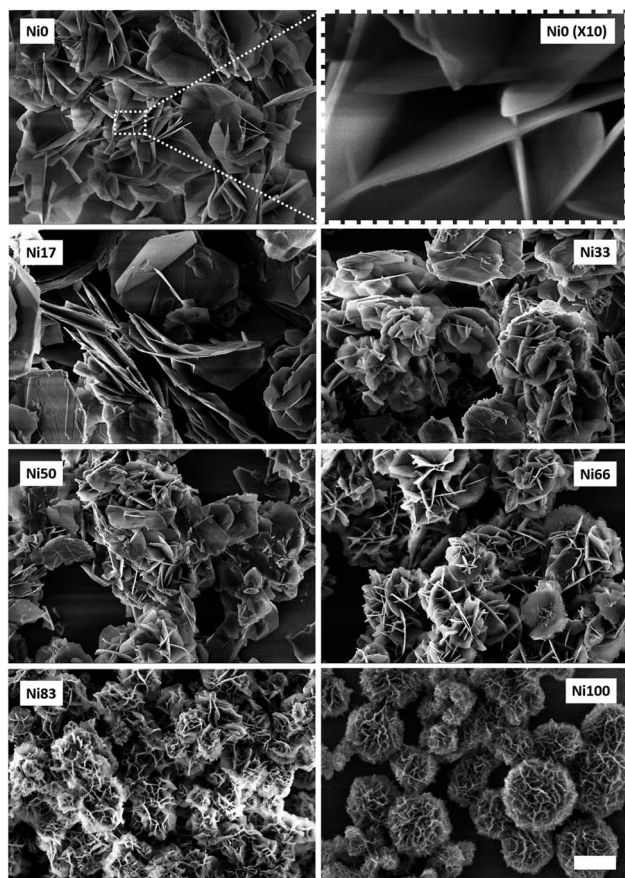

Fig. 2 FESEM images of Ni0 to Ni100 samples. Scale bar represents 2 μm for all images except the inset (upper row).
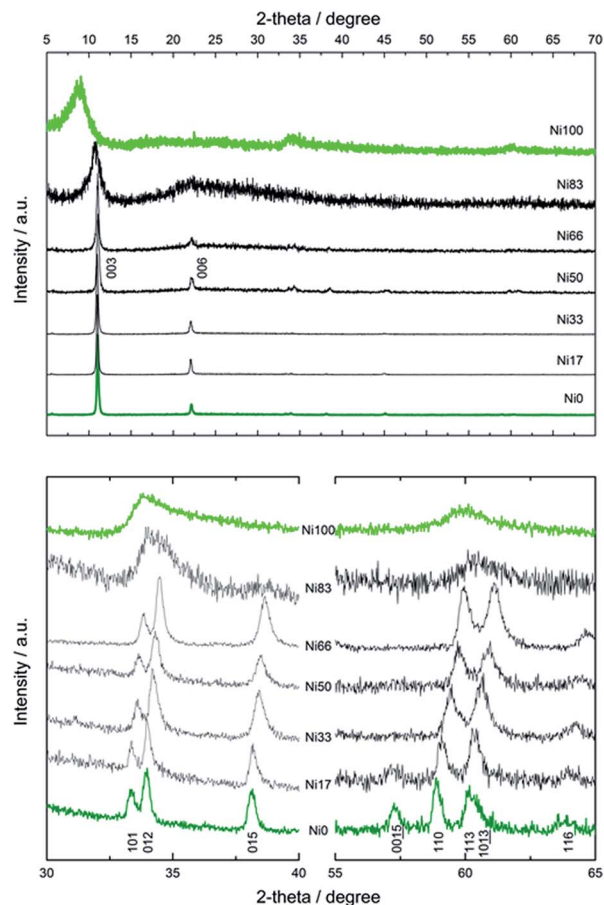

Fig. 3 Wide range PXRD patterns of Ni0 to Ni100 samples (upper panel) and detail of intralamellar reflections (lower panel).

tetrahedral Co(II) centers, Co^{Td}, positioned externally from the brucitic layer.[39] The typical green color of this phase obeys to the contribution of the inherent transitions of Co(II) centers present in four-fold and six-fold coordination environments. In contrast with the Zn(II)-based mineral simonkolleite,[38] that is defined by the precise formula $Zn^{Oh}_{0.75}Zn^{Td}_{0.5}(OH)_{1.5}Cl \cdot nH_2O$, the fraction of tetrahedral positions depends on the preparation method and is still a matter of discussion.[40] However, the composition obtained under the present method is fully coincident with reports dealing with more energetic aging conditions.[41] Ni(II)-rich samples resemble to bare Ni(II) end member also known as alpha hydroxide; this phase consists of a turbostratic lamellar hexagonal lattice obeying to the formula $Ni(OH)_{2-x}(A)_x \cdot nH_2O$, where A^- represents an exchangeable anion,[36] with Ni(II) centers located in octahedral environment, exclusively.[42–44] This layered compound has the ability to exchange anions as related layered double hydroxides, despite the absence of trivalent cations in the structure.[45] This ill-crystallized phase typically depicts broad interlamellar reflection due to the small thickness along the c direction and the inherent deformation of the nanoflakes.

Fig. 4 presents the dependence of interlamellar distance $c/3$, deduced from 003 and 006 reflections as well as intralamellar cation to cation distance a, proportional to the 110 plane. For both end members, Ni0 and Ni100, the observed parameters are coincident with the chloride containing alpha forms reported before.[39] In the case of sample Ni0, the replacement of Co^{Oh} positions by pairs of Co^{Td}, results in a net contraction of the a parameter of 0.02 Å respect to the characteristic a value of pure brucitic or beta $Co(OH)_2$. The contraction of sample Ni100 respect to reference beta $Ni(OH)_2$ is in good agreement with previous reports.[46] In the composition range in which the mixed phase adopts the simonkolleite-like structure, the interlamellar distance remains invariant while the cation to cation average distance contracts with increasing Ni(II) contents, confirming the inclusion of Ni(II) ions within the structure.[46] Then, the structure observed for samples Ni0 to Ni66 can be described as a simonkolleite-like alpha structure according

to the $(Ni,Co)^{Oh}_{1-x}Co^{Td}_{2x}(OH)_{2-2x}(Cl)_2 \cdot nH_2O$ formula.[47] On the other side of the phase diagram, samples Ni83 and Ni100 resulted in ill-crystallized turbostratic alpha phase $(Ni,Co)^{Oh}_{1-x}(OH)_{2-x}(Cl)_x \cdot nH_2O$.

Electrochemical performance of all samples was evaluated by means of cyclic voltammetry (CV) and galvanostatic charge–discharge (CD) measurements, at increasing potential sweeping rates and specific currents, respectively. The CV curves show the expected peaks for the redox reaction of Ni(II) and Co(II) in the potential window resulting in the pseudocapacitance behavior of the faradic processes. Samples were cycled at 50 mV s^{-1} until reproducible voltammograms were obtained. A stable response was reached after up to 15 cycles, depending on the Ni content of the samples. Fig. 5 shows the CV recorded for the all samples at a sweep rate of 2 mV s^{-1}; the complete set of CV plots are presented in Fig. S2.† The peaks observed for the binary samples lay between the potentials registered for the Ni0 and Ni100 end members. From sample Ni66 to Ni83 there is a change in the peaks shape, clearly noticeable in the forward scan. Moreover, for the bare Ni(II) sample, the presence of a pair of peaks can be discerned suggesting the occurrence of two redox processes for this sample, in agreement with recent findings.[48] It is accepted that Ni(II) hydroxide evolves to Ni(III) oxohydroxide in a single electron conversion. Then, the complex signal observed suggest the coexistence of alpha and beta forms of Ni(II) hydroxide;[49] steps are being taken in order to elucidate the origin of the observed peaks. In the CD plots (see ESI Fig. S3†), the pseudocapacitance behavior due to the electrochemical adsorption–desorption or surface redox reaction is represented by the non-linear discharge curves.

The specific capacitance (C_s) obtained from the CV and CD for the various composition at the different experimental conditions are presented as 3D plots in Fig. 6. Both techniques find a maximum C_s value in sample Ni83; CD reflects a C_s maximum value of 2100 ± 20 F g^{-1} for this sample. Related brucitic $Ni_{0.8}Co_{0.2}(OH)_2$ solid solutions revealed a similar C_s value to Ni83, however once the discharge current density was increased to 8 A g^{-1}, this value decreased to
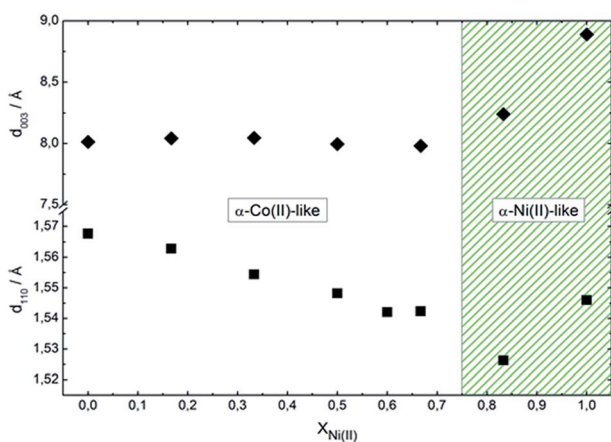

Fig. 4 Dependence of interlayer (003) and intralayer (110) distance as a function of composition. White region depict the prevalence of simonkolleite-like structure (α-Co(II)-like) while green region the prevalence of turbostratic (α-Ni(II)-like) one.
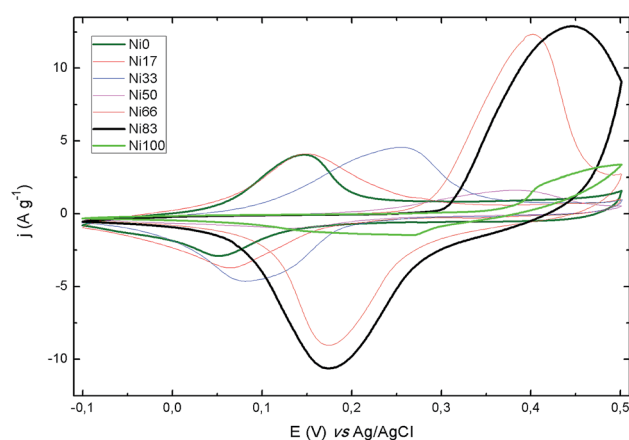

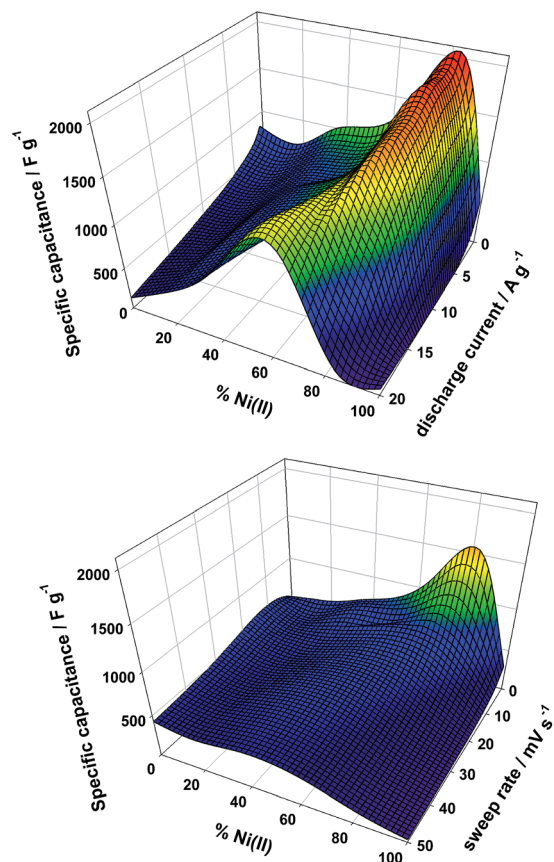**Fig. 5** Voltammograms of all prepared samples recorded at 2 mV s^{-1} vs. Ag/AgCl electrode.

Fig. 6 3D plot of specific capacitance as a function of composition obtained from CD plots (top graph) and CV plots (bottom graph).

Fig. 7 Ragone plot for the prepared samples calculated from the CV measurements.

a half.[50] Sample Ni83 retains 90% of C_s as the specific discharged current is increased up to 16 A g^{-1}. Higher rates displace the optimum value to sample Ni66 with a marked decrease of C_s to 1500 F g^{-1} (Fig. 6, top graph). In contrast with this robust behavior, CV determinations reflect a lower C_s maximum value of 1500 F g^{-1} followed by a continuous decay and a shift towards Ni33 sample when the sweep rate increases (Fig. 6, bottom graph). Interestingly, Co(II) rich compositions maintains the C_s with the sweep rate, suggesting that these samples presents less kinetic hindrances for the redox-mediated phase transitions than their Ni(II) rich counterparts. The optimum performance recorded lie among the best values reported for related phases.[51]

Fig. 7 shows the Ragone plot for all the samples at the various scan rates recorded; the values of E and P are in the expected region for the supercapacitors. The maximum specific energy is observed for sample Ni83 with 80.7 ± 0.8 W h kg^{-1} at specific power of 960 ± 9 W kg^{-1} followed by the composition Ni66 with a specific energy of 60.2 ± 0.6 W h kg^{-1} at a specific power of 717 ± 7 W kg^{-1}. Cobalt-rich samples present a narrow range in specific energy while the compositions rich in Ni(II) show a narrow range in specific power. The samples around equimolar compositions (Ni33–66) stand intermediate of the aforementioned behaviors indicating that for those
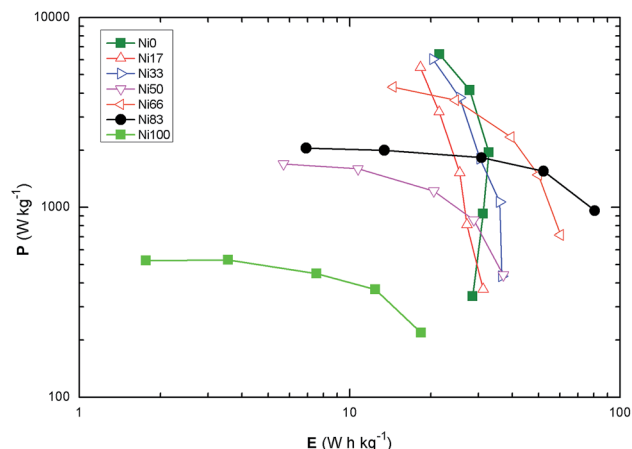
compositions there must be a change in the surface structure leading to the results of specific capacitance.

Conclusions

Epoxide's route allows the quantitative coprecipitation of layered monophasic Co(II)–Ni(II) hydroxides in the whole range of compositions, without the occurrence of undesired beta phases. Due to the absence of hydrothermal ripening, pristine born micrometric crystalline platelets preserve their nanometric thickness, along the c direction, ensuring a proper reactivity. Despite the layered crystalline structure of the obtained samples, two different phases can result, depending on the Co(II) to Ni(II) ratio. A simonkolleite-like structure, characterized by the coexistence of Oh and Td environments prevails for $X_{Ni(II)} \leq 0.66$. For $X_{Ni(II)}$ equal or higher than 0.83, a layered turbostratic phase is obtained. Beyond this structural differences, a continuous electrochemical performance is observed, finding an optimum value for samples with $X_{Ni(II)} = 0.83$. The high values recorded suggest that the parent micrometric particles are able to massively convert along the redox cycles, reaching the performance of complex nano-textured related systems. Marked differences were observed for the maximum specific capacitances recorded, depending on the evaluation method and/or protocol employed.[51] This fact warns about the necessity of a wide range screening, in order to properly characterize this key electrochemical parameter.

Experimental

Synthesis

Typically, precipitations were driven by aging for 48 h at 298 K 100 cm^3 of filtered solutions containing NaCl (80 mM), a chloride salt of Co(II), Ni(II), or a combination of the aforementioned divalent cations (keeping a total cationic concentration of 10 mM) in the presence of glycidol (800 mM). All reagents were purchased from Sigma-Aldrich and employed without further

purification. The precipitated solids were collected by centrifugation, washed three times with cold water, and dried at room temperature.

Precipitation pH profiles

Representative precipitation curves were obtained by *in situ* potentiometric pH measurement in a reactor at 298 K under permanent stir constantly purged with N_2, in order to prevent atmospheric CO_2 uptake.

Characterization of solids

All synthesized solids were characterized by powder X-ray diffraction (PXRD) using a graphite-filtered Cu K$_\alpha$ radiation ($\lambda = 1.5406$ Å), field emission scanning electron microscopy (FESEM), equipped with energy dispersive X-ray spectroscopy (EDS) probe. The content of cations, chloride and water were assessed by ICP, ionic chromatography and elemental analysis, respectively.

Electrochemical characterization

The electrochemical properties of the obtained alpha hydroxides based electrodes were assessed in a three-electrode cell configuration at 25 °C. The hydroxides were deposited over the working electrode (WE), consisting of a graphite disk (5 mm in diameter). A mixture of the hydroxides (80%) with acetylene black (Cabot) (10%) and PVDF (Sigma Aldrich, powder) (10%) in *N*-methyl-2-pyrrolidone (Sigma Aldrich, anhydrous 99.5%), was prepared, deposited over the electrode and dried under vacuum until constant weight. Cyclic voltammetry (CV) and galvanostatic charge–discharge (CD) measurements, were performed with an Autolab PGSTAT302N (Metrohm, Netherlands) in 1 M KOH aqueous solution employing a Ag/AgCl electrode as reference electrode (RE) and a coiled Pt wire (150 × 0.5 mm, Vega y Camji, 99.9%) as a counter electrode (CE). CV were performed between −0.1 V to 0.5 V *vs.* Ag/AgCl at sweeping rates of 2 mV s^{-1} to 50 mV s^{-1} while the CD were performed in a potential window of 0.0 V to 0.45 V *vs.* Ag/AgCl at specific currents ranging from 0.5 A g^{-1} to 20 A g^{-1}. The specific capacitance (C_s/F g^{-1}) of the nanoparticles were calculated from the CV and the CD curves. From the CV, by the formula $C_s = Q/(\Delta V \times m)$ where Q (C) is the charge, ΔV (V) is the potential window employed and m (g) the mass of the active material on the electrode. The capacitance was calculated as a half of the charge integer of the whole voltammogram. The capacitance from the CD curves was calculated by the formula: $C_s = I \times \Delta t/(\Delta V \times m)$, where I (A) is the discharge current, Δt (s) is the discharge time, ΔV (V) is the potential change during the discharge (excluding the *IR* drop) and m is again the mass of the active materials on the electrode.

The energy and power densities of the electrodes were calculated from the CVs. At the various sweep rates by the equations: $E = 0.5 \times C_s \times V^2$ and $P_{ave} = E \times t^{-1}$, where E (J g^{-1}) is the energy density, V (V) is the potential window, C_s (F g^{-1}) the specific capacitance, P_{ave} (J s^{-1} g^{-1}) is the average power density, and t (s) is time corresponding to the potential window.[7] E and P were converted to W h kg^{-1} and W kg^{-1}, respectively.

References

1 E. Umeshbabu, G. Rajeshkhanna and G. R. Rao, *Int. J. Hydrogen Energy*, 2014, **39**, 15627–15638.
2 L. Demarconnay, E. Raymundo-Piñero and F. Béguin, *Electrochem. Commun.*, 2010, **12**, 1275–1278.
3 J. R. Miller and P. Simon, *Science*, 2008, **321**, 651–652.
4 P. Simon and Y. Gogotsi, *Nat. Mater.*, 2008, **7**, 845–854.
5 S. Liu, S. Sun and X.-Z. You, *Nanoscale*, 2014, **6**, 2037–2045.
6 L. Cao, F. Xu, Y. Y. Liang and H. L. Li, *Adv. Mater.*, 2004, **16**, 1853–1857.
7 G. Wang, L. Zhang and J. Zhang, *Chem. Soc. Rev.*, 2012, **41**, 797–828.
8 W. Deng, X. Ji, Q. Chen and C. E. Banks, *RSC Adv.*, 2011, **1**, 1171–1178.
9 J. P. Cheng, J. Zhang and F. Liu, *RSC Adv.*, 2014, **4**, 38893–38917.
10 F. Wang, S. Xiao, Y. Hou, C. Hu, L. Liu and Y. Wu, *RSC Adv.*, 2013, **3**, 13059–13084.
11 R. R. Salunkhe, S. H. Hsu, K. C. W. Wu and Y. Yamauchi, *Chemsuschem*, 2014, **7**, 1551–1556.
12 H. S. Huang, K. H. Chang, N. Suzuki, Y. Yamauchi, C. C. Hu and K. C. W. Wu, *Small*, 2013, **9**, 2520–2526.
13 B. P. Bastakoti, H. Oveisi, C. C. Hu, K. C. W. Wu, N. Suzuki, K. Takai, Y. Kamachi, M. Imura and Y. Yamauchi, *Eur. J. Inorg. Chem.*, 2013, 1109–1112.
14 W. Chaikittisilp, M. Hu, H. J. Wang, H. S. Huang, T. Fujita, K. C. W. Wu, L. C. Chen, Y. Yamauchi and K. Ariga, *Chem. Commun.*, 2012, **48**, 7259–7261.
15 B. P. Bastakoti, Y. Kamachi, H. S. Huang, L. C. Chen, K. C. W. Wu and Y. Yamauchi, *Eur. J. Inorg. Chem.*, 2013, 39–43.
16 V. Gupta, S. Gupta and N. Miura, *J. Power Sources*, 2008, **175**, 680–685.
17 J. Han, K. C. Roh, M. R. Jo and Y.-M. Kang, *Chem. Commun.*, 2013, **49**, 7067–7069.
18 H. Chen, L. Hu, M. Chen, Y. Yan and L. Wu, *Adv. Funct. Mater.*, 2014, **24**, 934–942.
19 G. V. Manohara, D. A. Kunz, P. V. Kamath, W. Milius and J. Breu, *Langmuir*, 2010, **26**, 15586–15591.
20 H. Cai, A. C. Hillier, K. R. Franklin, C. C. Nunn and M. D. Ward, *Science*, 1994, **266**, 1551–1555.
21 U. Costantino, F. Marmottini, M. Nocchetti and R. Vivani, *Eur. J. Inorg. Chem.*, 1998, 1439–1446.

22 H. Cai, A. C. Hillier, K. R. Franklin, C. C. Nunn and M. D. Ward, *Science*, 1994, **266**, 1551–1555.

23 M. Ogawa and H. Kaiho, *Langmuir*, 2002, **18**, 4240–4242.

24 P. Benito, M. Herrero, C. Barriga, F. M. Labajos and V. Rives, *Inorg. Chem.*, 2008, **47**, 5453–5463.

25 M. Jobbagy, M. A. Blesa and A. E. Regazzoni, *J. Colloid Interface Sci.*, 2007, **309**, 72–77.

26 J. M. Oh, S. H. Hwang and J. H. Choy, *Solid State Ionics*, 2002, **151**, 285–291.

27 X. H. Liu, R. Z. Ma, Y. Bando and T. Sasaki, *Adv. Mater.*, 2012, **24**, 2148–2153.

28 V. Oestreicher, I. Fábregas and M. Jobbágy, *J. Phys. Chem. C*, 2014, **118**, 30274–30281.

29 V. Oestreicher and M. Jobbágy, *Langmuir*, 2013, **29**, 12104–12109.

30 A. E. Gash, T. M. Tillotson, J. H. Satcher, J. F. Poco, L. W. Hrubesh and R. L. Simpson, *Chem. Mater.*, 2001, **13**, 999–1007.

31 A. E. Gash, T. M. Tillotson, J. H. Satcher, L. W. Hrubesh and R. L. Simpson, *J. Non-Cryst. Solids*, 2001, **285**, 22–28.

32 A. E. Gash, J. H. Satcher and R. L. Simpson, *J. Non-Cryst. Solids*, 2004, **350**, 145–151.

33 A. E. Gash, J. H. Satcher and R. L. Simpson, *Chem. Mater.*, 2003, **15**, 3268–3275.

34 H. D. Zhang, B. Li, Q. X. Zheng, M. H. Jiang and X. T. Tao, *J. Non-Cryst. Solids*, 2008, **354**, 4089–4093.

35 L. Ehrenberg and S. Hussain, *Mutat. Res.*, 1981, **86**, 1–113.

36 G. Soler-Illia, M. Jobbagy, A. E. Regazzoni and M. A. Blesa, *Chem. Mater.*, 1999, **11**, 3140–3146.

37 K. Okamoto, N. Iyi and T. Sasaki, *Appl. Clay Sci.*, 2007, **37**, 23–31.

38 F. C. Hawthorne and E. Sokolova, *Can. Mineral.*, 2002, **40**, 939–946.

39 R. Z. Ma, Z. P. Liu, K. Takada, K. Fukuda, Y. Ebina, Y. Bando and T. Sasaki, *Inorg. Chem.*, 2006, **45**, 3964–3969.

40 J. R. Neilson, B. Schwenzer, R. Seshadri and D. E. Morse, *Inorg. Chem.*, 2009, **48**, 11017–11023.

41 Z. P. Liu, R. Z. Ma, M. Osada, K. Takada and T. Sasaki, *J. Am. Chem. Soc.*, 2005, **127**, 13869–13874.

42 M. Taibi, N. Jouini, P. Rabu, S. Ammar and F. Fievet, *J. Mater. Chem. C*, 2014, **2**, 4449–4460.

43 M. Taibi, S. Ammar, N. Jouini, F. Fievet, P. Molinie and M. Drillon, *J. Mater. Chem.*, 2002, **12**, 3238–3244.

44 K. I. Pandya, W. E. Ogrady, D. A. Corrigan, J. McBreen and R. W. Hoffman, *J. Phys. Chem.*, 1990, **94**, 21–26.

45 P. V. Kamath, G. H. Annal Therese and J. Gopalakrishnan, *J. Solid State Chem.*, 1997, **128**, 38–41.

46 J. B. Liang, R. Z. Ma, N. B. O. Iyi, Y. Ebina, K. Takada and T. Sasaki, *Chem. Mater.*, 2010, **22**, 371–378.

47 C. Tessier, L. Guerlou-Demourgues, C. Faure, A. Demourgues and C. Delmas, *J. Mater. Chem.*, 2000, **10**, 1185–1193.

48 J. Yan, Z. Fan, W. Sun, G. Ning, T. Wei, Q. Zhang, R. Zhang, L. Zhi and F. Wei, *Adv. Funct. Mater.*, 2012, **22**, 2632–2641.

49 P. Oliva, J. Leonardi, J. F. Laurent, C. Delmas, J. J. Braconnier, M. Figlarz, F. Fievet and A. Deguibert, *J. Power Sources*, 1982, **8**, 229–255.

50 G. Chen, S. S. Liaw, B. Li, Y. Xu, M. Dunwell, S. Deng, H. Fan and H. Luo, *J. Power Sources*, 2014, **251**, 338–343.

51 H. Chen, F. Cai, Y. Kang, S. Zeng, M. Chen and Q. Li, *ACS Appl. Mater. Interfaces*, 2014, **6**, 19630–19637.